Research Article

Phase transition and heterogeneous strengthening mechanism in CoCrFeNiMn high-entropy alloy fabricated by laser-engineered net shaping via annealing at intermediate-temperature

Yunjian Bai [a,c], Heng Jiang [a,c], Kuo Yan [a], Maohui Li [e], Yanpeng Wei [b,c], Kun Zhang [a,c,*], Bingchen Wei [a,c,d,*]

[a] Key Laboratory of Microgravity (National Microgravity Laboratory), Institute of Mechanics, Chinese Academy of Sciences, Beijing 100190, China
[b] Key Laboratory for Mechanics in Fluid Solid Coupling Systems, Institute of Mechanics, Chinese Academy of Sciences, Beijing 100190, China
[c] School of Engineering Science, University of Chinese Academy of Sciences, Beijing 100049, China
[d] Center of Materials Science and Optoelectronics Engineering, University of Chinese Academy of Sciences, Beijing 100049, China
[e] Institute of Quartermaster Engineering & Technology, Academy of System Engineering, Academy of Military Sciences, Beijing 100010, China

ABSTRACT

High-entropy alloys (HEAs) have attracted tremendous attention owing to their controllable mechanical properties, whereas additive manufacturing (AM) is an efficient and flexible processing route for novel materials design. However, a profound appraisal of the fundamental material physics behind the strengthening of AM-printed HEAs upon low/intermediate-temperature annealing is essential. In this work, CoCrFeNiMn HEAs have been prepared using laser-engineered net shaping (LENS) and subsequently annealed at different temperatures. The CoCrFeNiMn HEA annealed at intermediate-temperature (873 K) exhibits a strong strain hardening capability, resulting in ultimate strength of 725 MPa and plasticity of 22%. A ternary heterogeneous strengthening mechanism is proposed to explain this phenomenon, in which equiaxed grains, columnar grains, and σ precipitates play different roles during tensile deformation. The resultant excellent strength and ductility can be ascribed to the heterostructure-induced mismatch. The equiaxed grains provide adequate grain boundaries (GBs), which induce dislocation plugging-up and entanglement; the columnar grains induce the onset and arrest of the dislocations for plastic deformation; and the σ precipitates hinder the movement of slip dislocations. The results provide new insights into overcoming the strength-ductility trade-off of LENS-printed HEAs with complex geometries.

© 2021 Published by Elsevier Ltd on behalf of Chinese Society for Metals.

1. Introduction

Additive manufacturing (AM) is a disruptive technology that promises to fabricate industrial products with complex geometries. The process consists of printing successive layers of materials on top of each other. It creates products from a 3D model data with complex shapes and low materials waste, which is widely used in the traditional engineering field such as laser sintering, laser melting and laser metal deposition [1]. Despite these advantages, the choice of structural printable materials for AM is limited to steel [2-4], Ti [5], Al [6,7], Ni alloys [8] and metallic glass systems [9,10]. Most investigated materials exhibit a notable defect density induced by the printing process, which must be minimized by additional thermal-mechanical treatments or special process control methods [6,8]. A more thorough understanding of the connections between the raw materials, process parameters and mechanical properties is desirable to acquire the satisfied products without defects and unreliable performances [11].

High-entropy alloys (HEAs) have attracted exceptional attention to material scientists due to their unique properties, such as excellent high strength [12], corrosion resistance [13], and high-temperature stability [14]. HEAs usually possess at least five elements in approximately equiatomic proportions with a high mixing entropy [15]. They tend to form a single crystalline structure rather than complex intermetallic compounds. Due to the large differences in atomic sizes between the constituent elements and strong lattice distortion, HEAs exhibit regulable strength-ductility combinations, which may make them promising candidates for different industrial fields.

Traditional methods for manufacturing HEAs use two main methods to improve their performance: one is to tailor the el-

emental composition and/or ratio during the manufacturing process; the other is to perform annealing and recrystallization at a high temperature on as-cast parts that have undergone severe plastic deformation (e.g., cold rolling). For example, the HEA $Al_xCoCrFeNiMn$ was studied in terms of the effect of its Al content on the structure evolution and mechanical properties [16]. As the Al content increases, the structure of this HEA begins to transform from FCC to BCC, thereby achieving a transition from high ductility to high strength. Sun et al. [17] obtained ultra-fine grains ranging from about 500 nm to 35 μm in CoCrFeNiMn HEAs via cold rolling and annealing at various temperatures from 923 K to 1373 K, which helped them achieve a combination of higher yield strength (~888 MPa) and a comparable ductility (~21%) in this alloy.

All of the above reports improve the understanding of why HEAs exhibit a good strength-ductility synergy; however, bulk ingots HEAs products manufactured by conventional method exhibit inherent limitations with respect to irregular shapes, which restricts their further expansion and widespread utilization. Compared with traditional manufacturing methods, the LENS method provides greater promise for the explorations of HEA products. The ultrafast cooling rate of LENS is beneficial for microstructure refinement, and it also can inhibit the segregation of constituent elements, as well as the formation of undesired intermediate phases or intermetallic compounds in HEAs products [18]. Thus, it has opened a way to produce lightweight, customizable, and assembly-free printed HEA products for industrial applications [19]. Recently, material scientists have made lots of investigations to AM-printed HEAs. Sun et al. [20] explored a new method to inhibit hot tearing by grain boundary segregation during printing. They found that adding Al can significantly reduce hot cracks in CoCrFeNi HEA, owing to Al segregation-induced ordered B2 phase, and the inherent residual strain is transformed from tensile strain in CoCrFeNi to compressive strain in $Al_{0.5}CoCrFeNi$. In addition, Karthik et al. [21] made an in-depth research on heterogeneous aspects of AM-printed parts, including melt pool boundaries, heterogeneous grain structure, texture, etc. They found that the shallow molten pool would result in a ⟨011⟩ texture while the deep molten pool would result in ⟨001⟩ and ⟨011⟩ textures. Particularly, Moghaddam et al. [22] gave a detailed review to AM-printed HEAs, including various AM methods, strengthening mechanism, special structure, post treatment strategies, mechanical properties and valuable outlook. They pointed out that annealing, especially annealing at a high temperature, is the most common post treatment for AM-printed HEAs [22]. However, the AM-printed HEAs with complex shapes could not be cold processed or recrystallized with an excessive temperature like their as-cast counterpart. Thus, the low/intermediate-temperature heat treatment may become a new method for performance improvements.

In this paper, CoCrFeNiMn HEA was fabricated using a LENS-450 machine. The phase transition, microstructural evolution and tensile properties of the printed samples following annealing at different temperatures were reported systematically. Meanwhile, the strengthening mechanism of the sample annealed at intermediate-temperature (873 K) was also thoroughly investigated.

2. Experimental

The pre-alloyed powder of CoCrFeNiMn HEA was prepared by vacuum induction melting gas atomization using argon gas. To ensure a good flowability of the pre-powder during printing, the size distribution of the pre-powder was controlled in the range of 50–100 μm. The samples were manufactured using a LENS-450 machine with a laser beam diameter of 260 μm at a near-constant layer thickness of 25 μm. The laser power was controlled at 300 W, with a scanning speed of 500 mm/min. Argon

was utilized as the protecting gas nourished through the beam path in the powder feed nozzle. Cubic bulk HEA specimens with 5 mm × 5 mm × 10 mm for microstructure analysis were printed layer-by-layer on a steel substrate. Dog-bone-shaped specimens for tensile test with gage dimensions of 38 mm × 3 mm × 1.5 mm were directly fabricated to bypass the subsequent cutting process. A bidirectional scanning strategy was used, in which the scanning direction between the two adjacent layers was parallel. Figs. 1(a) and (b) shows the schematic diagram of the scanning strategy and the tensile specimens, respectively.

The printed samples were annealed at low- (673 K), intermediate- (873 K), and high- (1073 K) temperature for 2 h in an argon atmosphere respectively, followed by furnace cooling. X-ray diffraction with Cu $K\alpha$ radiation was utilized to identify the phase of all samples, using step-by-step scanning (2°/min) to more accurately determine the diffraction peak positions. The scanning electron microscope equipped with backscattered diffraction (EBSD) was used to characterize all samples before and after fracture. To remove surface defects, dog-bone-shaped specimens were polished using 600, 1000, and 2000-grit SiC paper. The tensile tests were performed at a steady strain rate of 5 × 10^{-4} s^{-1} under room temperature on an Instron 5565 machine, and an extensometer with a displacement resolution of 0.1 μm was utilized to measure the elongation.

3. Results and discussion

3.1. XRD pattern analysis

Fig. 2(a) illustrates the XRD patterns of the pre-powder, as well as printed samples before and after annealing at various temperatures. Fig. 2(b) shows an enlargement of the (111) diffraction peaks of all samples. Compared with the pre-powder sample, the as-printed sample contains only a single FCC mono-structure, except for changes in the (111) texture from the abnormal peak intensity ratio, in agreement with previous findings [23-27]. Moreover, the (111) peak of the as-printed sample shifts from 43.49° to 43.75° compared with that of the pre-powder due to residual stress induced by lattice distortion during printing [1,28,29]. After annealing at low temperature, the sample remains as a single FCC structure. However, the (111) peak shifts left compared with the as-printed pattern, which is probably attributed to residual stress relief during annealing. After annealing at intermediate-temperature, the XRD pattern shows a significant difference compared with the as-printed sample: firstly, the highest intensity diffraction peak changes from (111) to (200); secondly, the σ phase appears at $2\theta = 46°$, indicating the decomposition of the FCC matrix in the sample. The formation of σ phase has also been reported when annealing at an intermediate temperature [30-32]. However, after annealing at high temperature, the highest intensity diffraction peak of the sample reverts to the (111) peak, and no obvious σ phase is detected. The disappearance of the σ phase has also been found in the as-cast CoCrFeNiMn HEA when the annealing temperature exceeded 1073 K [32]. Additionally, the (111) peak detected in this sample shifts to the right and broadens compared with the as-printed sample, indicating a decreased (111) inter-planar spacing and a refined grain size.

Fig. 2(c) depicts the lattice parameters of all samples. The lattice parameter of the powder is 0.360 nm, while the lattice parameter of the as-printed sample is lower (0.358 nm), likely due to the accumulation of a large amount of residual compressive stress during the printing process. It may have also occurred due to the volatilization of Mn which has the lowest boiling point. The lattice parameter of the printed sample annealed at low-temperature increases to 0.369 nm due to residual stress relief during annealing, whereas that of the sample annealed at intermediate-temperature
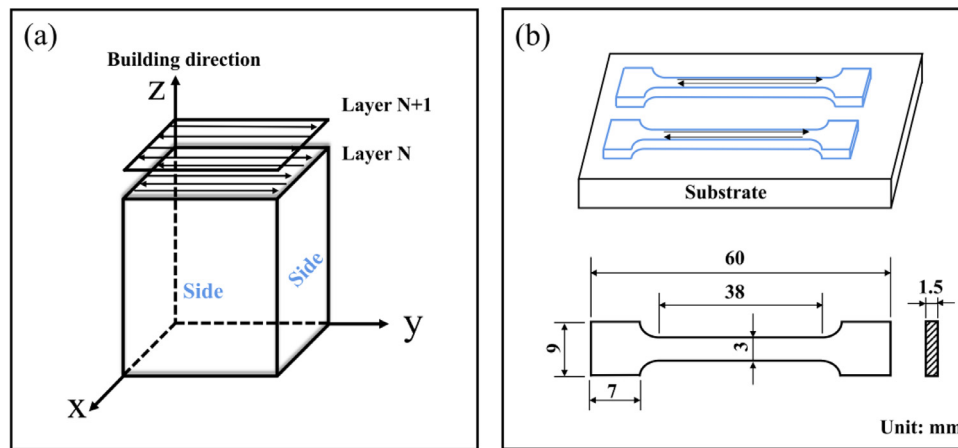
Fig. 1. Schematic diagram of (a) the scanning strategy and (b) tensile specimen.
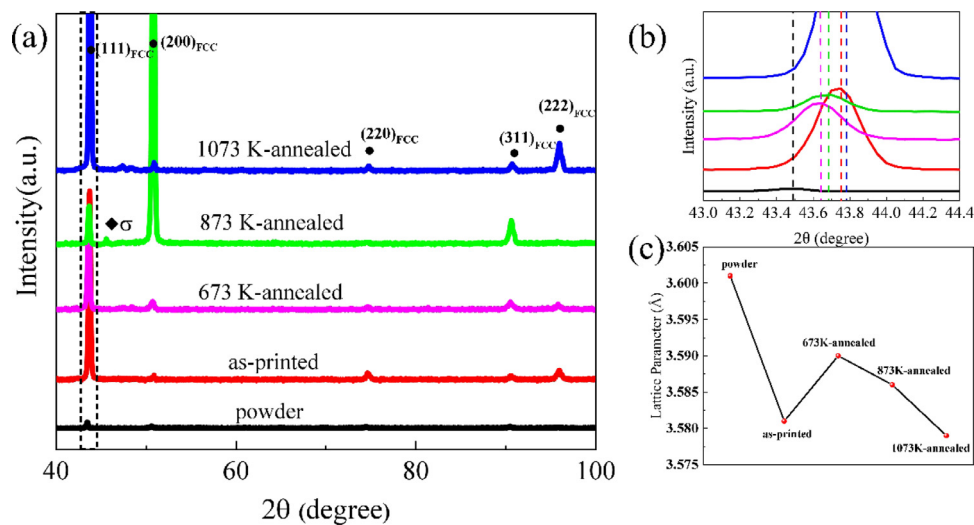

Fig. 2. (a) XRD patterns of all samples. (b) The enlarged image of the (111) diffraction peaks. (c) The (111) lattice parameters of different samples.

only increases to 0.359 nm, which may be ascribed to σ phase precipitation. However, the lattice parameter of the sample annealed at high-temperature becomes almost the same as that of the as-printed sample due to recrystallization.

3.2. Microstructure analysis

To investigate the structural evolution of printed samples before and after annealing at different temperatures, the grain distributions determined by EBSD are provided. Fig. 3(a-d) shows the grain map with side views, where the color represents the orientation of the corresponding grain to distinguish adjacent grains. Fig. 3(e-h) shows the combination map of grain boundary and phase distribution. The criterion of 15° is used to distinguish low-angle GBs (LAGBs) marked by red solid lines from high-angle GBs (HAGBs) marked by black solid lines. As can be found in Fig. 3(a), the structure of the as-printed sample is composed of equiaxed and columnar grains, in good agreement with previous results [24-26,33-35]. The average size of the equiaxed grains is estimated to be about 12 μm based on HAGBs, whereas columnar grains possess widths from a few to hundreds of micrometers, as can be seen in Fig. 3(e). The growth direction of the columnar grains is almost perpendicular to the molten pool boundaries marked by white dashed lines, which is due to the epitaxial grain growth along the maximum thermal gradient direction [36]. In addition, Fig. 3(e) shows that

the as-printed sample contains a high fraction (17%) of LAGBs, similar to the results of Zhu et al. [34] and Chew et al. [35]. At the same time, the corresponding phase distribution map shows that no second phase precipitates.

After annealing at low-temperature, the structure of this sample shows an analogous grain distribution, except for the molten pool boundary, which turns into a little unbent as shown in Fig. 3(b). Moreover, the distinction between equiaxed GBs and columnar GBs becomes less clear in Fig. 3(f), which may be attributed to the growth of columnar grains induced by grain boundary migration [37]. When the annealing temperature increases to 873 K, the structure of the intermediate-temperature annealed sample exhibits nearly straight molten pool boundaries compared with that of the as-printed sample in Fig. 3(c). Besides, the σ phase marked by the blue area appears on the FCC matrix (gray area). Further observation reveals that the σ phase precipitates at the dense equiaxed GBs adjacent to the columnar GBs as shown in Fig. 3(g). There may be two reasons for this phenomenon: firstly, the fine equiaxed GBs exhibit much faster kinetics than coarse GBs and thus, they can preferentially serve as nucleation sites for the second phase [31], which explains why σ phase appears at the dense equiaxed GBs; secondly, there is a large stress field at or near the interface between equiaxed grains and columnar grains due to mismatches in their elastic moduli and/or deformability. This stress would act as a driving force to induce σ
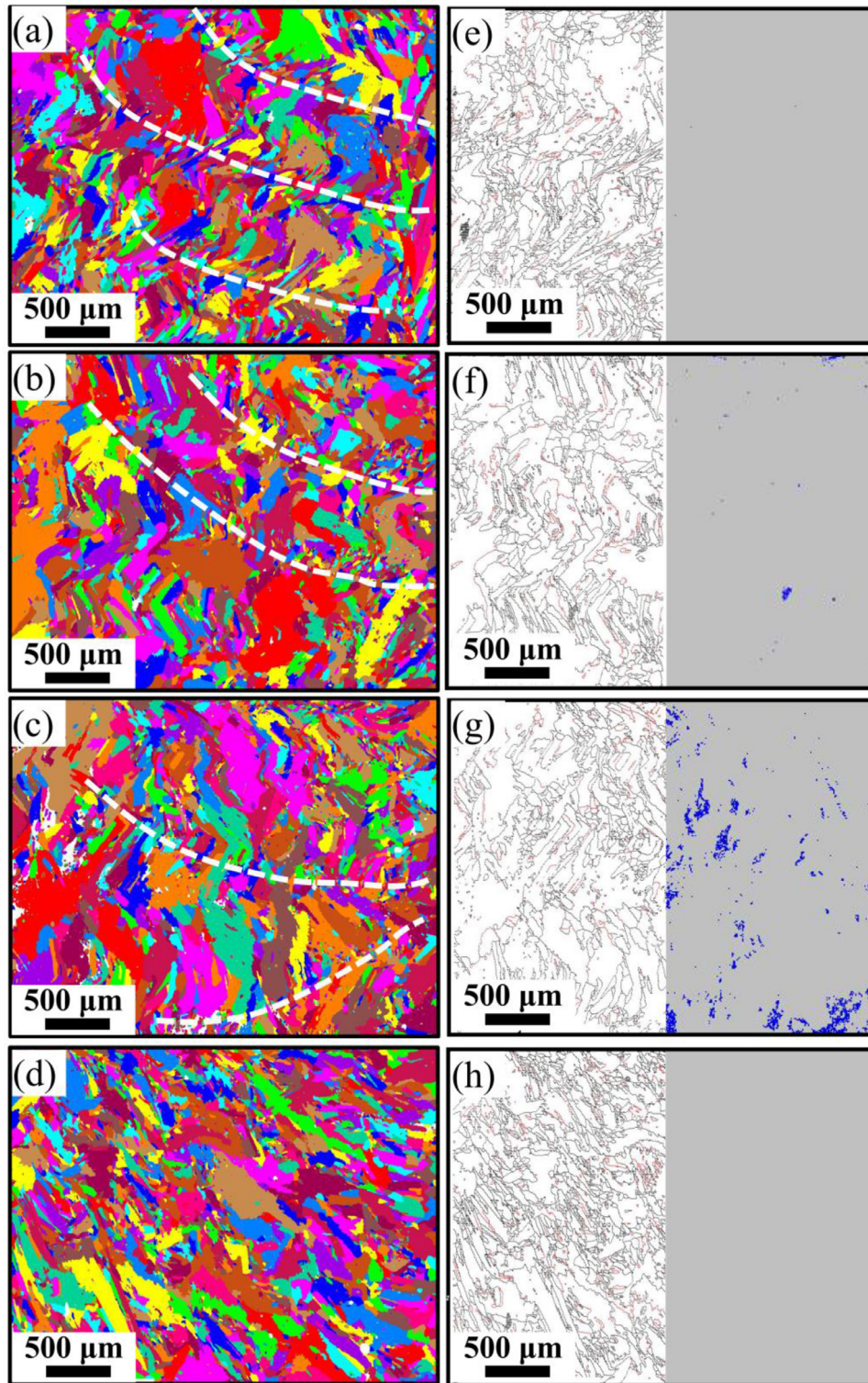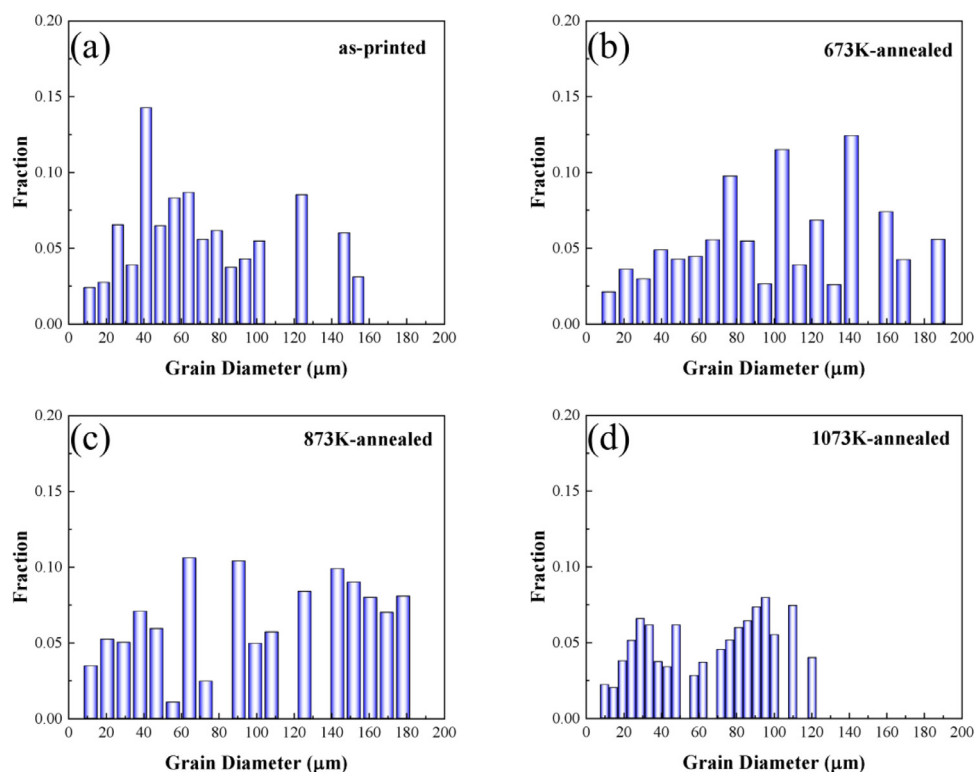
Fig. 3. The average grain color map of (a) the as-printed sample and that annealed at (b) low-temperature, (c) intermediate-temperature, and (d) high-temperature, respectively. The combination map of grain boundary and phase distribution of (e) the as-printed sample and that annealed at (f) low-temperature, (g) intermediate-temperature, and (h) high-temperature, respectively.

phase precipitation, which is why σ phase precipitates at equiaxed GBs adjacent to columnar GBs. Namely, the precipitation of σ phase is the result of coupling between thermodynamics and kinetics.

However, the sample annealed at high-temperature exhibits essential differences from the as-printed sample. There are obvious

grain refinement regions and no visible molten pool boundaries, as shown in Fig. 3(d). In particular, the fraction of equiaxed GBs is significantly higher than the others, and it is difficult to distinguish equiaxed-columnar grains from the GBs as shown in Fig. 3(h). This phenomenon indicates that dynamic recrystallization occurred in this sample, which verifies the XRD results.

Fig. 4. The columnar grain distributions of the as-printed sample (a) and that annealed at (b) low-temperature, (c) intermediate-temperature, (d) high-temperature, respectively.

As shown in Fig. 3, the equiaxed grains do not change significantly before and after annealing. However, the columnar grains show obvious differences and hence, to further reveal the evolution of columnar grains in the printed sample before and after annealing at various temperatures, the histograms of columnar grain distributions of all samples are provided in Fig. 4.

Fig. 4(a) shows that the diameters of columnar grains vary from a few to about 160 μm which is consistent with the findings through GBs in Fig. 3(e). Particularly, the size of columnar grains is mainly distributed in dozens of micrometers scale. After annealing at low-temperature, the size of partial columnar grains exceeds to 160 μm, which means an obvious grains' growth, as can be seen in Fig. 4(b). Fig. 4(c) depicts the distribution of columnar grains in the sample annealed at intermediate-temperature, which has the same trend as that of the one annealed at low-temperature. Moreover, compared with Fig. 4(b), Fig. 4(c) shows a more uniform distribution of those columnar grains, of which diameter is between 140 μm and 180 μm and hence, this sample possesses a unique equiaxed grains-columnar grains-precipitates ternary heterogeneous structure. When the annealing temperature is high, however, due to the dynamic recrystallization, the columnar grains exhibit an obvious refinement, and there are almost no grains larger than 120 μm, as shown in Fig. 4(d).

3.3. Residual stress analysis

To explore the effect of residual stress on changes in the equiaxed-columnar grains and phase transition, the lattice distortion characterized by kernel average misorientation (KAM) map and corresponding local misorientation (LM) map is shown in Fig. 5, which is typically used to indicate the plastic deformation in specimens [38-40]. In this work, the KAM map is used to reflect the residual stress in printed CoCrFeNiMn HEA samples. Here, the darker the color in the KAM map, the higher the lattice distortion, and the higher the corresponding residual stress.

The color representing the degree of residual deformation is relatively uniform in Fig. 5(a), indicating that overall distortion is induced by residual stress in the as-printed sample. The corresponding LM map (Fig. 5(e)) shows that the average misorientation is about 0.74°. This result indicates that there is large residual stress in the as-printed sample; otherwise, the average misorientation should be zero or close to zero, ideally. After annealing at low-temperature, a light-colored (blue) region appears in Fig. 5(b), meaning that residual deformation recovery occurred during heat treatment. It also indicates that the average residual stress decreased in this sample, which manifests as the average misorientation decreasing from 0.74° to 0.70° in Fig. 5(f). However, after annealing at intermediate-temperature, this sample exhibits obvious changes in local misorientation due to σ phase precipitated. As displayed in Fig. 5(c), in the area where the σ phase precipitates, the color is extremely dark, indicating strong lattice distortion due to phase transformation [41]. This is reasonable since the different crystal structures before and after the σ phase transformation would inevitably lead to large local misorientation, and large residual stress would be generated to accommodate this strain. Furthermore, the generation of σ phase may increase deformation in adjacent columnar grains, and the distortion in grains far from σ phase is low. Due to the large local misorientation, the average misorientation increases to 0.88° as shown in Fig. 5(g), and the amplitude decreases due to the discrete distribution of residual stress. However, the color in the sample annealed at high temperature becomes relatively uniform again, meaning that recrystallization produces a uniform stress distribution, as shown Fig. 5(d). According to the views of Wang et al. [42], the residual stress is grain-orientation dependent and may be re-distributed after annealing. The reduction in orientation anisotropy of residual stress may be due to the dynamic recrystallization.
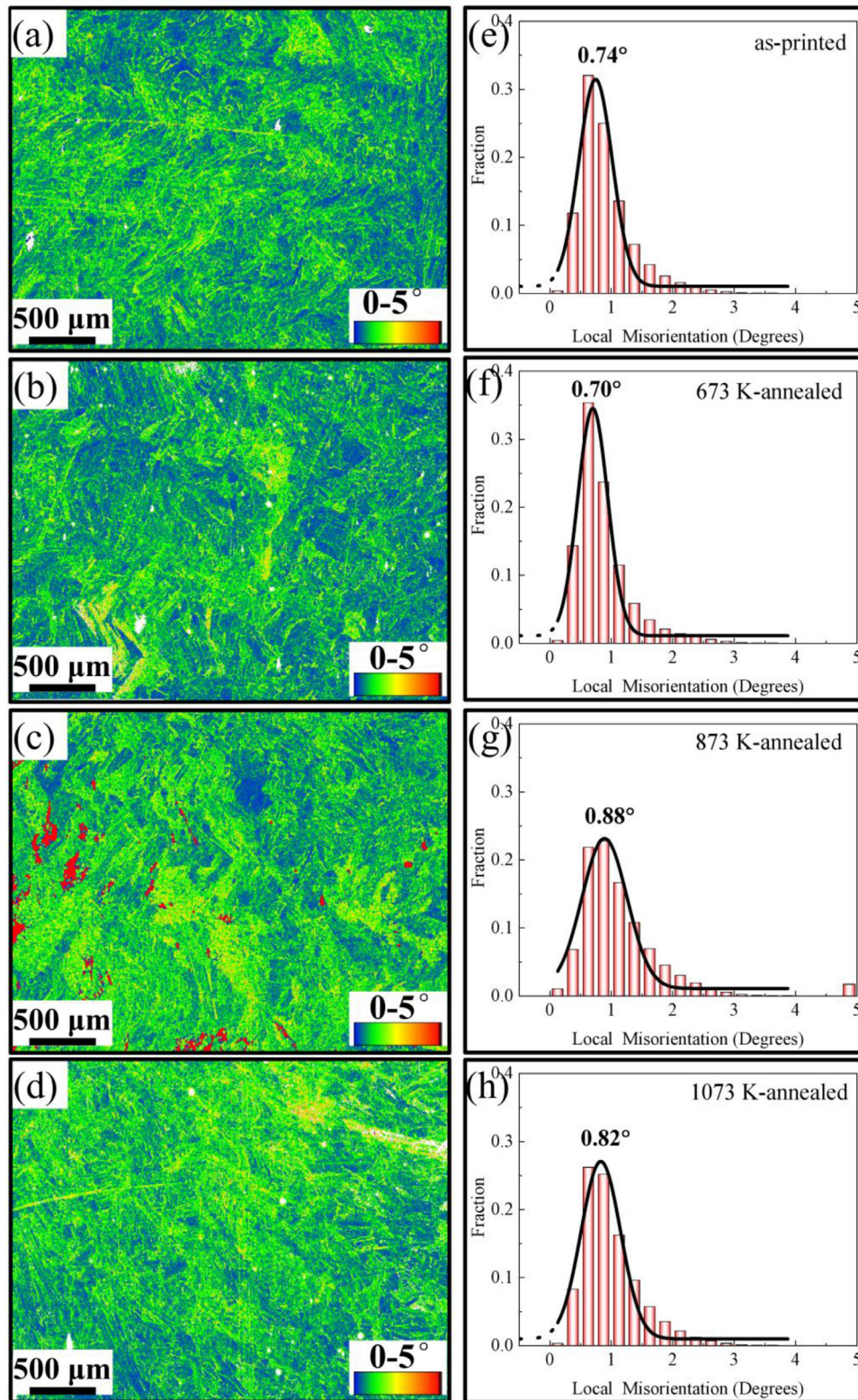
Fig. 5. KAM maps of (a) the as-printed simple and that annealed at (b) low-temperature, (c) intermediate-temperature, and (d) high-temperature, respectively. And the LM maps of (e) the as-printed simple and that annealed at (f) low-temperature, (g) intermediate-temperature, and (h) high-temperature, respectively.

3.4. Tensile properties and strengthening mechanism

3.4.1. Tensile properties

Fig. 6(a) displays the tensile behavior of the printed samples before and after annealing at various temperatures, and the mea-

sured yield strength (σ_y), ultimate strength (σ_{UTS}), and elongation (E_f) in this work are summarized in Table 1. The σ_y, σ_{UTS}, and E_f of the as-printed sample are 499 MPa, 666 MPa, and 18%, respectively. The σ_y, σ_{UTS}, and E_f of both samples annealed at low- and intermediate-temperature, are higher, possibly due to resid-
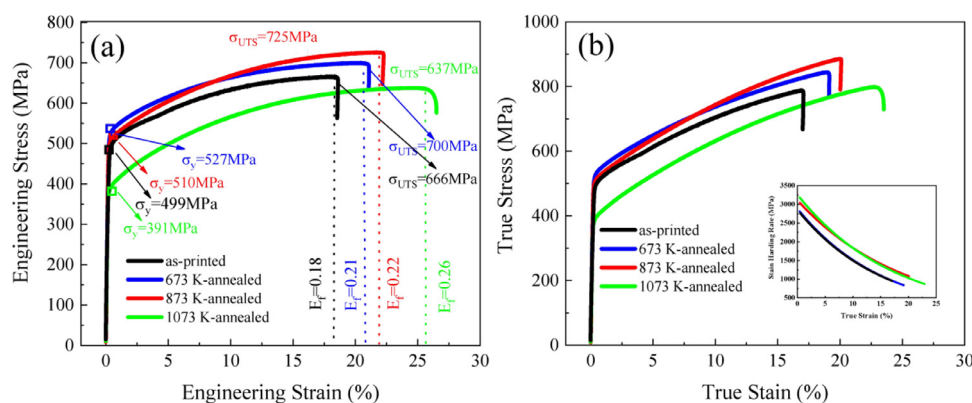
Fig. 6. (a) The typical engineering tensile stress-stain curves of all samples. (b) The corresponding true stress-strain curves of (a), and the inset is the strain hardening rate.

Table 1
Tensile properties of the CoCrFeNiMn HEA in this work.

Sample	σ_y (MPa)	σ_{UTS} (MPa)	E_f (%)
As-printed	499	666	18
673 K	527	700	21
873 K	510	725	22
1073 K	391	637	26

ual stress relief during heat treatment. In particular, the sample annealed at intermediate-temperature possesses the highest σ_{UTS} of 725 MPa along with a σ_y of 510 MPa, which is comparable to that of the one annealed at low-temperature (σ_y =527 MPa). Thus, this sample displays a greater strain hardening capability. The sample annealed at high-temperature shows an obvious softening phenomenon in which σ_y and σ_{UTS} are lower than the others, while E_f is the highest.

To investigate the strain hardening capability of all samples, the true stress-strain curves derived from Fig. 6(a) are presented in Fig. 6(b), where the inset reflects the strain hardening rate. The strain hardening rate curves of all samples possess the same trend in which, upon increasing deformation, the instantaneous strain hardening capabilities of all samples gradually decrease, yielding a banana-like curve. The curve of the sample annealed at intermediate-temperature almost coincides with that belonging to the one annealed at high-temperature, and it is higher than that belonging to the as-printed sample and the one annealed at low-temperature throughout the entire tensile deformation. However, the sample annealed at intermediate-temperature exhibits a higher strength and therefore, this sample possesses the best strength-ductility synergy.

3.4.2. Strengthening mechanism

The strengthening mechanism of materials with heterostructure may be complicated due to the multi-scale grains, hetero-domains, and different crystal structures, etc. Sun et al. [43, 44] used the finite strain crystal plasticity model to simulate hierarchical martensitic steel with grain-packet-block microstructure, and they proved in a theoretical way that the block and packet boundaries strongly influence the local response [44]. Thus, it is important to identify the role of equiaxed grains, columnar grains, and σ precipitates during the tensile test to understand the strengthening mechanism deeply. Fig. 7 shows the EBSD results of the sample annealed at intermediate-temperature after fracture. Compared with Fig. 3(c), most grains (especially columnar grains) are rotated by aligning to the tensile axis (TA), as shown in Fig. 7(a). Figs. 7(e) and (f) are the inverse pole figures (IPF) of equiaxed grains and columnar grains, respectively. The equiaxed grains exhibit no obvious tex-

ture, while the columnar grains exhibit a (111) fiber texture. More interestingly, many slip bands marked by black arrows are found in the columnar grains, which are absent in equiaxed grain regions. Generally, slip bands can be viewed as a typical characteristic of dislocation gliding [45], where the mechanism is a typical columnar grain-dominated deformation mode. Fig. 7(b) depicts the phase distribution of this sample after fracture. The fraction of σ precipitates increases from 2.2% to 6.8%, implying that the nucleation and growth of these precipitates are accompanied during the tensile test. The KAM map of this sample after fracture shows a higher misorientation angle than that in the as-printed state. Moreover, the larger KAM values (red spots) are located at GBs, especially where the equiaxed GBs are dense. In fact, the larger the KAM value, the more severe the deformation, indicating that lots of dislocations gathered at the equiaxed GBs. Because of the multi-scale grains and the hetero-domains between the FCC matrix and σ phase (i.e., the equiaxed-columnar-precipitates ternary heterostructure), geometrically necessary dislocations (GNDs) are produced to collaborative deformation. As can be seen in Fig. 7(c), there are many GNDs located at the GBs between equiaxed grains and columnar grains. Far from the GBs, the density of GNDs in the columnar grains gradually decreases, which is expressed as the blue color.

There is a consensus that coarse grains can accommodate larger dislocations due to their larger size. Accordingly, coarse-grained structures tend to display better uniform plastic deformation capabilities, whereas fine-grained structures can store limited dislocations, which inevitably inhibit plastic deformation. On the other hand, fine-grained structures often contain more GBs than coarse-grained structures, and these GBs would become the preferred locations for dislocation plugging up and entanglement, which favors forest strengthening. Therefore, dislocation-dislocation interactions and dislocation-grain boundary interactions can improve the strength and deteriorate the ductility.

Fig. 8 shows a schematic diagram of the sample annealed at intermediate-temperature during tensile deformation. Fig. 8(a) illustrates the initial morphology of equiaxed grains (EG) and columnar grains (CG), where 2.2% of the initial σ phase precipitates at the dense equiaxed GBs adjacent to the columnar boundaries. During deformation, dislocations are mainly generated in the columnar grains, which is rare in equiaxed grains. The difference in the dislocation storage capacity between coarse columnar grains and fine equiaxed grains leads to strain incompatibility at equiaxed-columnar interfaces where a strain gradient appears. GNDs are thus produced near equiaxed-columnar interfaces to assist with compatible deformation as shown in Fig. 8(b). According to Li et al. [46], these GNDs finally block the motion of other slip dislocations to form bundles of concentrated dislocations (BCDs),
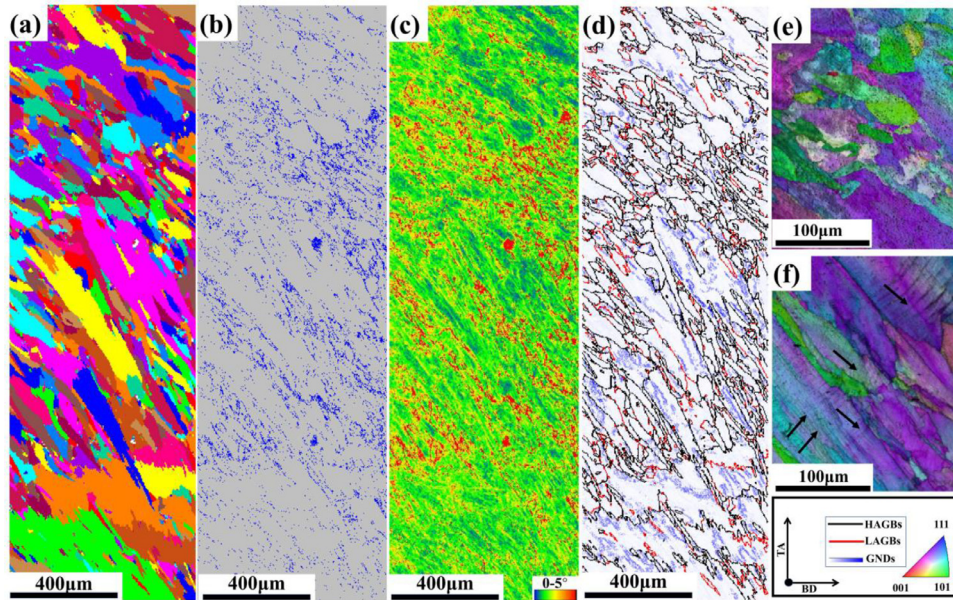
Fig. 7. EBSD results of the sample annealed at intermediate-temperature after fracture: (a) grain map, (b) phase distribution map, (c) KAM map, (d) grain boundary map, and IPF of (e) equiaxed grains and (f) columnar grains.
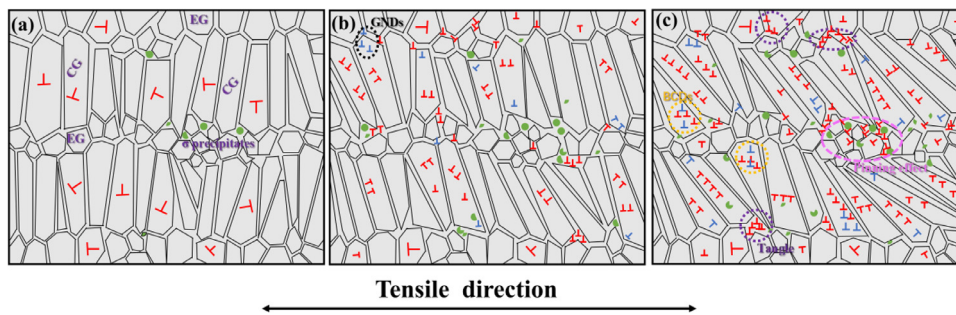

Fig. 8. The schematic illustration of the sample annealed at intermediate-temperature: (a) before deformation, (b) during deformation, and (c) after deformation.

which is beneficial for additional hardening. At the same time, the σ phase increases due to deformation and finally reaches 6.8%. The σ precipitates lead to strong interactions between slip dislocations and dislocation tangles, which impede dislocation motion in columnar grains and result in a pinning effect in equiaxed GBs, as depicted in Fig. 8(c). This improves the σ_{UTS} of this sample; therefore, the σ_{UTS} in our study can be expressed as follows:

$$\sigma_{UTS} = \sigma_0 + \Delta\sigma_{p1} + \Delta\sigma_{p2} \qquad (1)$$

where σ_0 represents the intrinsic ultimate strength of the printed sample, and $\Delta\sigma_{p1}$ and $\Delta\sigma_{p2}$ represent the additional ultimate strength provided by the σ phase in columnar grains and equiaxed GBs, respectively. Since the σ phase is hard and brittle, $\Delta\sigma_{p1}$ can be estimated by the Ashby-Orowan relation, as follows:

$$\Delta\sigma_{p1} = 0.538(Gbf^{1/2}/d)\ln(d/2b) \qquad (2)$$

where G represents the shear modulus, b represents the burgers vector, f represents the volume fraction of the σ precipitates embedded in columnar grains and d represents the diameter of the σ precipitates.

However, as mentioned previously, plastic deformation is mainly borne by the columnar grains, and the existence of the σ phase does not significantly inhibit its deformation, so this sample maintains good ductility. Therefore, the ternary heterogeneous strengthening leads to good stain hardening capability and additional strengthening without deteriorating the ductility. This pro-
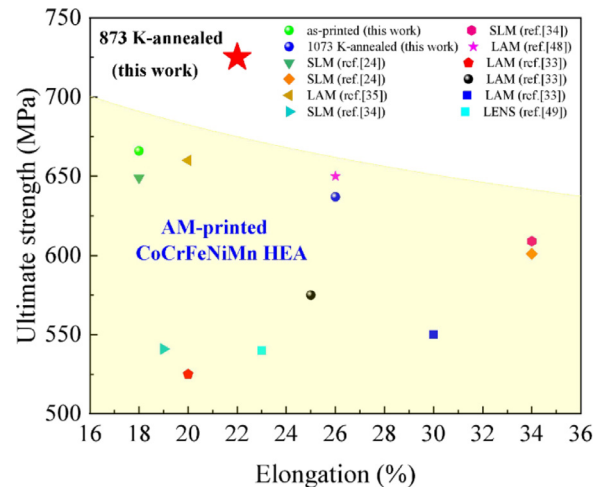

Fig. 9. Ultimate strength versus elongation-to-failure plot of AM-printed CoCrFeNiMn HEA.

ceeds via hetero-deformation induced (HDI) strain hardening proposed by Zhu and Wu [47], which produces a good combination of strength and ductility.

Fig. 9 plots the ultimate strength versus elongation in this work, as well as other AM-printed CoCrFeNiMn HEA [24, 33-35, 48, 49].

Clearly, the sample annealed at intermediate-temperature (873 K) in our work possesses an excellent combination of extremely high ultimate strength and good ductility due to its unique heterogeneous ternary structure.

4. Conclusion

We have demonstrated a strategy to enhance the performance of LENS-printed samples via annealing at different temperatures. The sample annealed at intermediate-temperature exhibits an excellent combination of high ultimate strength of 725 MPa and strain of 22%, which possesses dense equiaxed grains, 2.2% σ precipitates and a uniform distribution of relatively coarse columnar grains. After fracture, many slip bands are found in the columnar grain region, and the content of the σ precipitates increases to 6.8%. The combination of extremely high ultimate strength and considerable ductility can be attributed to the typical equiaxed grains-columnar grains-precipitates ternary heterogeneous structure. Specially, the columnar grains contain the dislocations required for deformation; the fine equiaxed grains provide a place for dislocations to pack and entangle; and the nucleation and growth of the σ precipitate during deformation further hinder the movement of slip dislocations. In addition, the excellent work hardening capability of this sample is ascribed to an HDI strain hardening mechanism, where the formation of GNDs may play a dominant role during tensile deformation. The results of this work may provide a new idea for improving the performance of AM-printed products.

Declaration of Competing Interest

Authors have no conflict of interest to declare.

Acknowledgments

References

[1] D.D. Gu, W. Meiners, K. Wissenbach, R. Poprawe, Int. Mater. Rev. 57 (2012) 133–164.
[2] A. Riemer, S. Leuders, M. Thöne, H.A. Richard, T. Tröster, T. Niendorf, Eng. Fract. Mech. 120 (2014) 15–25.
[3] J.A. Cherry, H.M. Davies, S. Mehmood, N.P. Lavery, S.G.R. Brown, J. Sienz, Int. J. Adv. Manuf. Technol. 76 (2014) 869–879.
[4] Z. Wang, T.A. Palmer, A.M. Beese, Acta Mater 110 (2016) 226–235.
[5] L. Thijs, F. Verhaeghe, T. Craeghs, J. Van Humbeeck, J.P. Kruth, Acta Mater 58 (2010) 3303–3312.
[6] I. Maskery, N.T. Aboulkhair, A.O. Aremu, C.J. Tuck, I.A. Ashcroft, R.D. Wildman, R.J.M. Hague, Mater. Sci. Eng. A 670 (2016) 264–274.
[7] P. Wang, J. Eckert, K.G. Prashanth, M.W. Wu, I. Kaban, L.X. Xi, S. Scudino, Trans. Nonferrous Met. Soc. China 30 (2020) 2001–2034.
[8] K. Moussaoui, W. Rubio, M. Mousseigne, T. Sultan, F. Rezai, Mater. Sci. Eng. A 735 (2018) 182–190.
[9] J.P. Best, H.E. Ostergaard, B. Li, M. Stolpe, F. Yang, K. Nomoto, M.T. Hasib, O. Muránsky, R. Busch, X. Li, J.J. Kruzic, Addit. Manuf. 36 (2020) 101416.
[10] Y. Lu, S. Su, S. Zhang, Y. Huang, Z. Qin, X. Lu, W. Chen, Acta Mater 206 (2021) 116–632.
[11] N. Li, S. Huang, G. Zhang, R. Qin, W. Liu, H. Xiong, J. Mater. Sci. Technol. 35 (2019) 242–269.
[12] X. Gao, Y. Lu, B. Zhang, N. Liang, G. Wu, G. Sha, J. Liu, Y. Zhao, Acta Mater 141 (2017) 59–66.
[13] Y. Shi, B. Yang, P.K. Liaw, Metals (Basel) 7 (2017) 1–18.
[14] O.N. Senkov, G.B. Wilks, D.B. Miracle, C.P. Chuang, P.K. Liaw, Intermetallics 18 (2010) 1758–1765.
[15] J.W. Yeh, S.K. Chen, S.J. Lin, J.Y. Gan, T.S. Chin, T.T. Shun, C.H. Tsau, S.Y. Chang, Adv. Eng. Mater. 6 (2004) 299–303.
[16] J.Y. He, W.H. Liu, H. Wang, Y. Wu, X.J. Liu, T.G. Nieh, Z.P. Lu, Acta Mater 62 (2014) 105–113.
[17] S.J. Sun, Y.Z. Tian, H.R. Lin, X.G. Dong, Y.H. Wang, Z.J. Zhang, Z.F. Zhang, Mater. Des. 133 (2017) 122–127.
[18] S. Chen, Y. Tong, P. Liaw, Entropy 20 (2018) 937.
[19] C. Han, Q. Fang, Y. Shi, S.B. Tor, C.K. Chua, K. Zhou, Adv. Mater. 32 (2020) 1903855.
[20] Z. Sun, X. Tan, C. Wang, M. Descoins, D. Mangelinck, S.B. Tor, E.A. Jägle, S. Zaefferer, D. Raabe, Acta Mater 204 (2021) 116505.
[21] G.M. Karthik, H.S. Kim, Met. Mater. Int. 27 (2021) 1–39.
[22] A.O. Moghaddam, N.A. Shaburova, M.N. Samodurova, A. Abdollahzadeh, E.A. Trofimov, J. Mater. Sci. Technol. 77 (2021) 131–162.
[23] S. Peng, S. Mooraj, R. Feng, L. Liu, J. Ren, Y. Liu, F. Kong, Z. Xiao, C. Zhu, P.K. Liaw, W. Chen, Scr. Mater. 190 (2021) 46–51.
[24] R. Li, P. Niu, T. Yuan, P. Cao, C. Chen, K. Zhou, J. Alloys Compd. 746 (2018) 125–134.
[25] X. Gao, Y. Lu, Mater. Lett. 236 (2019) 77–80.
[26] P. Wang, P. Huang, F.L. Ng, W.J. Sin, S. Lu, M.L.S. Nai, Z.L. Dong, J. Wei, Mater. Des. 168 (2019) 107576.
[27] J. Li, S. Xiang, H. Luan, A. Amar, X. Liu, S. Lu, Y. Zeng, G. Le, X. Wang, F. Qu, C. Jiang, G. Yang, J. Mater. Sci. Technol. 35 (2019) 2430–2434.
[28] Y. Li, K. Zhou, P. Tan, S.B. Tor, C.K. Chua, K.F. Leong, Int. J. Mech. Sci. 136 (2018) 24–35.
[29] P. Mercelis, J.P. Kruth, Rapid Prototyping J 12 (2006) 254–265.
[30] E.J. Pickering, R. Muñoz-Moreno, Scr. Mater. 113 (2016) 106–109.
[31] B. Schuh, F. Mendez-Martin, B. Völker, E.P. George, H. Clemens, R. Pippan, A. Hohenwarter, Acta Mater 96 (2015) 258–268.
[32] N.D. Stepanov, D.G. Shaysultanov, M.S. Ozerov, S.V. Zherebtsov, G.A. Salishchev, Mater. Lett. 185 (2016) 1–4.
[33] Z. Tong, X. Ren, J. Jiao, W. Zhou, Y. Ren, Y. Ye, E.A. Larson, J. Gu, J. Alloys Compd. 785 (2019) 1144–1159.
[34] Z.G. Zhu, Q.B. Nguyen, F.L. Ng, X.H. An, X.Z. Liao, P.K. Liaw, S.M.L. Nai, J. Wei, Scr. Mater. 154 (2018) 20–24.
[35] Y. Chew, G.J. Bi, Z.G. Zhu, F.L. Ng, F. Weng, S.B. Liu, S.M.L. Nai, B.Y. Lee, Mater. Sci. Eng. A 744 (2019) 137–144.
[36] D. Zhang, D. Qiu, M.A. Gibson, Y. Zheng, H.L. Fraser, D.H. StJohn, M.A. Easton, Nature 576 (2019) 91–95.
[37] Z.W. Zhang, G. Chen, G.L. Chen, Acta Mater 55 (2007) 5988–5998.
[38] M. Kamaya, K. Kubushiro, Y. Sakakibara, S. Suzuki, H. Morita, R. Yoda, D. Kobayashi, K. Yamagiwa, T. Nishioka, Y. Yamazaki, Y. Kamada, T. Hanada, T. Ohtani, Mech. Eng. J. 3 (2016) 16–00077.
[39] M.N. Gussev, K.J. Leonard, J. Nucl. Mater. 517 (2019) 45–56.
[40] A.A. Tiamiyu, M. Eskandari, M. Sanayei, A.G. Odeshi, J.A. Szpunar, Mater. Sci. Eng. A 673 (2016) 400–416.
[41] M. Calcagnotto, D. Ponge, E. Demir, D. Raabe, Mater. Sci. Eng. A 527 (2010) 2738–2746.
[42] Y.D. Wang, R.L. Peng, X.L. Wang, R.L. McGreevy, Acta Mater 50 (2002) 1717–1734.
[43] F. Sun, E.D. Meade, N.P. O'Dowd, J. Mech. Phys. Solids 113 (2018) 35–55.
[44] F. Sun, E.D. Meade, N.P. O'Dowd, Int. J. Plast. 119 (2019) 215–229.
[45] F. Weng, Y. Chew, Z. Zhu, X. Yao, L. Wang, F.L. Ng, S. Liu, G. Bi, Addit. Manuf. 34 (2020) 101202.
[46] J. Li, Q. Zhang, R. Huang, X. Li, H. Gao, Scr. Mater. 186 (2020) 304–311.
[47] Y. Zhu, X. Wu, Mater. Res. Lett. 7 (2019) 393–398.
[48] S. Guan, D. Wan, K. Solberg, F. Berto, T. Welo, T.M. Yue, K.C. Chan, Mater. Sci. Eng. A 761 (2019) 138056.
[49] Z. Qiu, C. Yao, K. Feng, Z. Li, P.K. Chu, Int. J. Lightweight Mater. Manuf. 1 (2018) 33–39.